Geobiology

Geobiology (2012), **10**, 347–354 DOI: 10.1111/j.1472-4669.2012.00329.x

Characterisation of the dissimilatory reduction of Fe(III)-oxyhydroxide at the microbe – mineral interface: the application of STXM–XMCD

V. S. COKER,[1] J. M. BYRNE,[1] N. D. TELLING,[2] G. VAN DER LAAN,[3] J. R. LLOYD,[1] A. P. HITCHCOCK,[4] J. WANG[5] AND R. A. D. PATTRICK[1]

[1]*School of Earth, Atmospheric & Environmental Sciences and Williamson Research Centre for Molecular Environmental Science, University of Manchester, Manchester, UK*
[2]*Institute for Science and Technology in Medicine, Keele University, Stoke-on-Trent, UK*
[3]*Diamond Light Source Ltd, Didcot, Oxfordshire, UK*
[4]*Brockhouse Institute for Materials Research, McMaster University, Hamilton, ON, Canada*
[5]*Canadian Light Source Inc., University of Saskatchewan, Saskatoon, SK, Canada*

ABSTRACT

A combination of scanning transmission X-ray microscopy and X-ray magnetic circular dichroism was used to spatially resolve the distribution of different carbon and iron species associated with *Shewanella oneidensis* MR-1 cells. *S. oneidensis* MR-1 couples the reduction of Fe(III)-oxyhydroxides to the oxidation of organic matter in order to conserve energy for growth. Several potential mechanisms may be used by *S. oneidensis* MR-1 to facilitate Fe(III)-reduction. These include direct contact between the cell and mineral surface, secretion of either exogenous electron shuttles or Fe-chelating agents and the production of conductive 'nanowires'. In this study, the protein/lipid signature of the bacterial cells was associated with areas of magnetite (Fe_3O_4), the product of dissimilatory Fe(III) reduction, which was oversaturated with Fe(II) (compared to stoichiometric magnetite). However, areas of the sample rich in polysaccharides, most likely associated with extracellular polymeric matrix and not in direct contact with the cell surface, were undersaturated with Fe(II), forming maghemite-like (γ-Fe_2O_3) phases compared to stoichiometric magnetite. The reduced form of magnetite will be much more effective in environmental remediation such as the immobilisation of toxic metals. These findings suggest a dominant role for surface contact-mediated electron transfer in this study and also the inhomogeneity of magnetite species on the submicron scale present in microbial reactions. This study also illustrates the applicability of this new synchrotron-based technique for high-resolution characterisation of the microbe–mineral interface, which is pivotal in controlling the chemistry of the Earth's critical zone.

Received 6 September 2011; accepted 24 February 2012

Corresponding author: V. S. Coker. Tel.: +44(0)161 275 3803; fax: +44(0)161 306 9361; e-mail: vicky.coker@manchester.ac.uk

INTRODUCTION

Microbial Fe(III) reduction is widespread in the subsurface and has significant environmental consequences, as it has been shown to control the mobility of radionuclides, toxic metals and organic molecules in many different environments (Lovley *et al.*, 2004). Therefore, it is of great interest to identify the precise mechanisms that dissimilatory Fe(III)-reducing bacteria use to reduce Fe(III)-bearing minerals. The Gram-negative, facultative anaerobe *Shewanella oneidensis* MR-1 is able to reduce solid-phase Fe(III) oxyhydroxides by coupling the reaction to the oxidation of organic matter (Lovley *et al.*, 1989; Nealson & Saffarini, 1994). This electron-transfer process can result in the formation of a range of Fe(II)-rich phases, including magnetite, green rusts, siderite or vivianite (Fredrickson *et al.*, 1998; Ona-Nguema *et al.*, 2002; Lloyd, 2003). As well as direct contact between cell surface and mineral, transferring electrons *via* outer membrane cytochromes (Myers & Myers, 1992; Shi *et al.*, 2007), there are a number of alternative methods that this bacterium can use to facilitate the electron-transfer process, particularly to reduce less bioavailable solid-phase minerals. These include the secretion of electron-shuttling compounds (Newman & Kolter, 2000; Marsili *et al.*, 2008; von Canstein *et al.*, 2008), the use

of endogenous electron shuttles such as humics (Newman & Kolter, 2000), the secretion of an Fe(III)-solubilising ligand (Taillefert *et al.*, 2007) and the production of electrically conducting pili or 'nanowires' (Gorby *et al.*, 2006; El-Naggar *et al.*, 2010). Here, we describe the use of the relatively novel and fast developing technique of scanning transmission X-ray microscopy (STXM) combined with X-ray magnetic circular dichroism (XMCD) to evaluate the spatial distribution of Fe(II) and Fe(III) vs. carbon signatures specific for a range of cellular macromolecules in Fe(III)-reducing cultures of *S. oneidensis* MR-1. This combination of STXM and XMCD has previously been used to identify the individual magnetic moment in magnetite nanocrystals in a magnetotactic bacterium (Lam *et al.*, 2010), and a comprehensive bibliography of STXM is available in Ade & Hitchcock (2008), with more recent updates available at http://unicorn.mcmaster.ca/xrm-biblio/xrm_bib.html. The direct visualisation of the oxidation state of Fe in both the extracellular and cell-surface environments gives a unique insight into the mechanism of Fe(III) reduction in this model organism. The study of this specific system has additional interest given the technological potential of the nanospheres of biomagnetite produced by this process and the ability to control their magnetic properties by the Fe(III)/Fe(II) behaviour (Coker *et al.*, 2009).

MATERIALS AND METHODS

Shewanella oneidensis MR-1 was grown under strictly anaerobic conditions at 30 °C in modified freshwater medium as described previously (Lloyd *et al.*, 2003). Sodium DL-lactate (100 mM) and fumarate (20 mM) were provided as the electron donor and acceptor, respectively. All manipulations were performed under an atmosphere of N_2–CO_2 (80:20). Poorly crystalline Fe(III)-oxyhydroxide was produced using the method of Lovley & Phillips (1986), where a 0.4 M solution of $FeCl_3$ is neutralised by 10 N NaOH to pH 7 and the solid then washed by centrifugation six times until no Cl^- ions remain. The mineral was stored in the dark at 4 °C for not more than 6 months before use. Late log-phase cultures of *S. oneidensis* MR-1 were harvested by centrifugation at 5000 *G* for 20 min and washed twice in carbonate buffer ($NaHCO_3$; 30 mM, pH 7.1) under N_2–CO_2 (80:20) prior to use. Aliquots of the washed cell suspension (0.5 mL) were added to sealed anaerobic bottles containing 9.9 mL bicarbonate buffer, 50 mM poorly crystalline Fe(III) oxide and 20 mM sodium lactate. The final concentration of bacteria corresponded to approximately 0.2 mg protein per mL. Bottles were incubated in the dark at 20 °C. After 1 week of incubation, an aliquot of the suspension (0.1 mL) was deposited and dried on a formvar-coated 3 mm 200-mesh copper grid (Agar Scientific, Stansted, UK) under anaerobic conditions. The grid was transferred on a sample holder from a glove bag to the STXM in an air-tight jar. The chamber contained an overpressure of N_2. The sample jar was only opened within the chamber, and the sample mounting was performed quickly to prevent sample oxidation. A second aliquot of sample was taken for powder X-ray diffraction (XRD) measurements. XRD measurements were obtained with a Bruker D8 Advance instrument using Cu $K_{\alpha 1}$ radiation. Data were acquired over the range 15°(2θ)–70°(2θ), using a step size of 0.02°(2θ).

Scanning transmission X-ray microscopy observations were carried out on the soft X-ray spectromicroscopy (SM) beamline BL 10ID1 of the Canadian Light Source (CLS) in Saskatoon, Canada. Observations were made firstly at the C *K*-edge followed by the Fe $L_{2,3}$-edge to minimise possible beam damage. The beamline has an energy resolving power $E/\Delta E > 3000$ and an incident flux of 10^8 ph/s/0.5 A at 3000 resolving power. Further details can be found in (Kaznatcheev *et al.*, 2007). The exit slits were adjusted such that the maximum flux used was 18 MHz. Energy calibration was achieved using the sharp peak for protein at 288.2 eV and the peak maximum for magnetite at 709.5 eV. Elemental maps (also called 'stack maps') were generated by taking a background image at 280 and 700 eV and subtracting this image from a corresponding image for C at 288.2 eV or Fe at 709.5 eV, respectively. Spectroscopic data were collected by scanning a spatial region of interest in *x*–*y* sample directions, perpendicular to the beam, at each energy increment over an energy range covering an elemental edge thus creating a spectrum at each pixel, known collectively as a stack (Jacobsen *et al.*, 2000). Care was taken to use as low a dose of X-rays as possible to minimise the impact of radiation damage on these measurements. This involved careful selection of dwell time, number of energy points and use of an automated fast, in-vacuum shutter, so only X-rays hitting the sample were contributing to the measured data. A dwell time of 0.95–1.15 ms was used, which has previously been shown to give minimal beam damage to samples containing a combination of iron minerals and bacteria (Miot *et al.*, 2009a). The energy step was 0.15 eV over the main features of each edge, and the image pixel size was 0.025 μm. Images at damage sensitive energies (289 eV in the C *K*-edge and 704 eV in the Fe $L_{2,3}$-edge) were measured after stack acquisitions; visible changes in the sample morphology were not noted.

The source point for the CLS–STXM is an elliptically polarising undulator (EPU), which provides nearly 100% circularly polarised light at the Fe $L_{2,3}$ edge (Kaznatcheev *et al.*, 2007). To determine the Fe $L_{2,3}$ XMCD, two image stacks were recorded in transmission mode for the same sample area, firstly with right circularly polarised (RCP) and then left circularly polarised (LCP) X-rays. A magnetic field of ~0.1 T was applied to the sample by mounting a strip of the grid between two poles of a magnet and having the sample plate at an angle of 30° to the beam direction, resulting in a component of the magnetic field parallel to the beam (see Fig. S1 for details). Data processing was carried out using the aXis2000 software package (Hitchcock, 2011). For both the C *K*-edge and Fe

$L_{2,3}$-edge, data transmission signals were converted to optical density (OD) units using the incident flux signals measured in the same stack through regions free of C or Fe, adjacent to regions of interest. Alignment of each stack was carried out in aXis2000 (Hitchcock, 2011) using the stack analyser function, which aligns images by cross-correlations using Fourier transforms. For the C *K*-edge, the image sequence was fitted using the singular value decomposition (SVD) method using standard spectra for expected components. Threshold masking was used to identify areas with similar spectral characteristics to the standards. For the Fe $L_{2,3}$-edge, the two stacks for the LCP and RCP X-rays are then added and ordered in photon energy and the alignment process repeated on the combined stack. The two well-aligned stacks are then separated again and subtracted to give a new stack that yields spectra that are the difference between the X-ray absorption spectra for RCP and LCP X-rays, in a magnetic field set at 30° to the incoming beam direction; XMCD spectra.

To obtain the relative amounts of the three Fe sites, the experimental spectra were fitted by means of a non-linear least-squares analysis, using calculated spectra for each of the Fe sites. In these calculations, as described by van der Laan & Thole (1991), the Hartree–Fock–Slater integrals for the $3d$-$3d$ and $2p$-$3d$ Coulomb and exchange interactions were scaled to 70 and 80%, respectively, and the crystal fields for the octahedral and tetrahedral sites were taken to be $10Dq$ = 1.4 and −0.6 eV, respectively. The calculated spectra were convoluted by a Lorentzian of Γ = 0.3 (0.5) eV for the L_3 (L_2)-edge to account for intrinsic core-hole lifetime broadening and by a Gaussian of σ = 0.2 eV to account for instrumental broadening. The experimental spectra were fitted over the L_3 main peaks only, which has been previously shown to give meaningful results, although fitting over the L_2 peak does give good qualitative agreement (Pattrick *et al.*, 2002).

RESULTS AND DISCUSSION

After 1 week of incubation with *S. oneidensis* MR-1, the orange Fe(III)-oxyhydroxide in the sample tubes had altered to a black magnetic precipitate, expected to be the Fe(II)-bearing mineral magnetite (Fe_3O_4) as reported previously (Coker *et al.*, 2007). This was subsequently confirmed using XRD (Fig. 1A), and the crystallite size of the magnetite was determined to be 29.15 ± 2.4 nm through fitting the (311) with a Lorentzian line shape and using the Scherrer equation. C *K* and Fe $L_{2,3}$-edge STXM analyses were performed on an aliquot of the sample slurry. First, the location of carbon-rich and iron-rich areas was mapped with an image step size of 0.05 μm across the sample to identify suitable areas for more in-depth analysis and to provide an overview of the spatial distribution of each element (Fig. 1B). It can be seen from Fig. 1B that there are oval/rod-shaped structures ~1 × 0.5 μm; comparison with previous images (Gorby *et al.*, 2006; Ravindranath *et al.*, 2011) and noting that they are

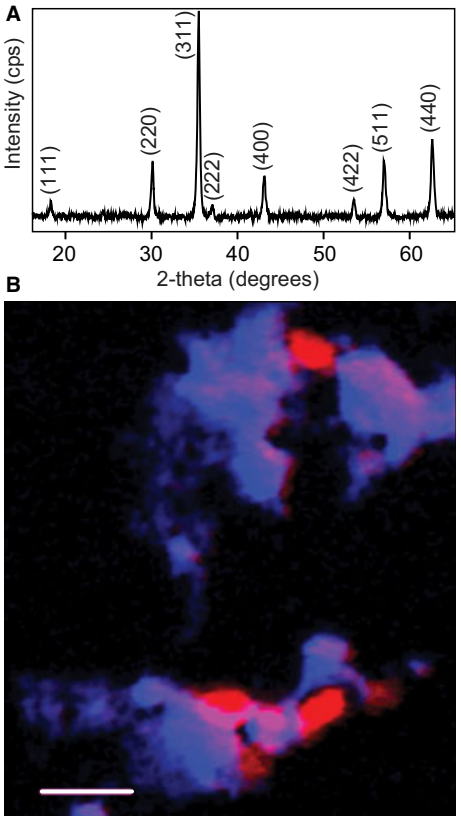

Fig. 1 (A) X-ray diffraction trace with the reflections for magnetite. (B) Colour composite of two scanning transmission X-ray microscopy maps (optical density, OD) measured at the C *K*-edge ($OD_{288.2}$–OD_{280}) in red and the Fe $L_{2,3}$-edge ($OD_{709.5}$–OD_{700}) in blue. 1 μm scale bar.

carbon-rich indicates they are cells of *S. oneidensis* MR-1, surrounded by deposits rich in iron, likely to be the magnetic precipitate.

A more detailed examination of the lower portion of the area represented by Fig. 1B was carried out by collecting images at regular energy intervals across the carbon *K*-edge between 280 and 320 eV, forming a 'stack' (see Materials and methods, above). SVD analysis using three standard spectra for protein, alginate and lipid, obtained from Lawrence *et al.* (2003), each normalised to an intensity corresponding to 1 nm thickness of the pure material (OD1), and a constant term was applied to the carbon *K*-edge stack. The areas of the sample containing high concentrations of protein (red), polysaccharide (green) or lipid (blue) are shown in Fig. 2A–C, with a colour composite image in Fig. 2D and the experimental spectra extracted for each of the three different components in Fig. 2E. The spectrum for areas containing a high concentration of protein gives a good fit to the standard spectrum from bovine serum albumin (BSA) containing both the $1s \rightarrow \pi^*_{C=C}$ transition at 285.1 eV and the main transition $1s \rightarrow \pi^*_{C=O}$ at 288.2 eV associated with the peptide bond (Lawrence *et al.*, 2003). The spectrum for areas of high lipid content also contains a large protein component, indicated by

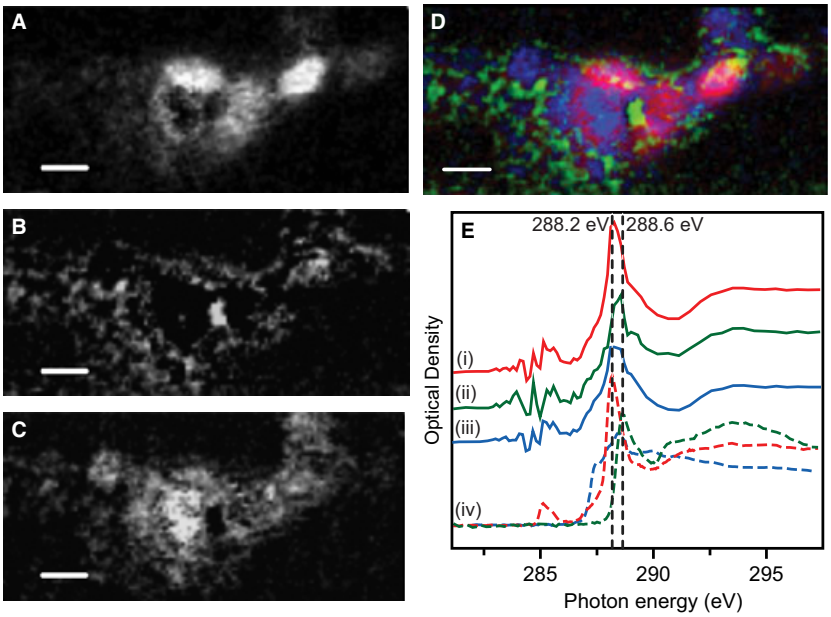

Fig. 2 Individual carbon component maps (A–C) derived by fitting an energy sequence of images (stack) of the C *K*-edge (96 images from 280 to 320 eV; 60 nm pixels, 1 ms per pixel) with a linear combination of albumin (protein) (A), alginate (polysaccharide) (B) and lipid (C). The maximum optical density (OD) values are 110 (A), 25 (B) and 70 (C). (D) Colour-coded composite map derived from images (A–C). Red = protein; green = polysaccharide; blue = lipid. (E) C *K*-edge spectra (i) protein, (ii) alginate and (iii) lipid extracted from the image stack (solid lines), compared to the reference standards (iv-using the same colours) used to generate the component maps (dotted lines) (from Lawrence *et al.*, 2003). Scale bar is 500 nm for all images.

the decrease in the intensity at 290.8 eV, demonstrating that the lipid-rich areas are also protein-rich. The protein and lipid signals come primarily from the oval/rod shapes ~1 × 0.5 μm, strongly supporting that these structures are cells of *S. oneidensis* MR-1. The polysaccharide spectrum gives a good agreement with the standard for alginate with the most intense peak associated with carboxyl groups (Benzerara *et al.*, 2004; Chan *et al.*, 2009) occurring at 288.6 eV, a distinctly higher energy than the 1s → $\pi^*_{C=O}$ at 288.2 eV of protein. From the component map (Fig 2B) and the colour-coded composite (Fig. 2D), the polysaccharide appears to surround the bacterial cell. This is consistent with a diffuse extracellular matrix of polysaccharide.

The distribution of Fe(II) and Fe(III), over the same region for the C *K*-edge, was examined in detail by collecting images and spectral data at energy intervals between 700 and 730 eV, creating a Fe $L_{2,3}$-edge stack. As magnetite contains both Fe(II) and Fe(III), in a 1:2 ratio, a linear regression analysis of the data using standard spectra for Fe(II) and Fe(III) was not practical for spatially resolving the differences in amounts and spatial distributions for the two oxidation states [see Fig. 3Ai,ii for the X-ray absorption spectral (XAS) shapes] because they are too closely associated within the sample. Therefore, XMCD spectral measurements were made as these have previously been shown to resolve the three Fe environments present in magnetite; the Fe(II) octahedral, Fe(III) tetrahedral and Fe(III) octahedral (Pattrick *et al.*, 2002; Morrall *et al.*, 2003), where each electronic state of Fe has a distinctly different XMCD spectral signature (see Fig. 3Aiii,iv for the XMCD spectral shapes).

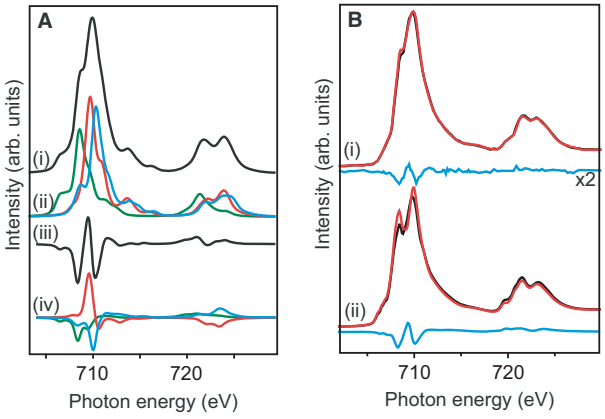

Fig. 3 (A) Calculated X-ray absorption spectral (XAS) (i) and X-ray magnetic circular dichroism (XMCD) (iii) spectra for the Fe $L_{2,3}$-edge of stoichiometric magnetite and individual components of the XAS (ii) and XMCD (iv) spectral calculations, Fe(II) octahedral (green), Fe(III) tetrahedral (red) and Fe(III) octahedral (blue). (B) Fe $L_{2,3}$-edge spectra for *Shewanella oneidensis* MR-1 nanomagnetite (i) XAS taken using left (red) and right (black) circularly polarised X-rays for the area within the yellow contour of Fig. 4 and the corresponding XMCD spectrum ×2 (blue); (ii) XAS taken in – (red) and + (black) 0.6 T magnetic field (Coker *et al.*, 2007) and the corresponding XMCD spectrum (blue).

The *S. oneidensis* MR-1 biomagnetite sample plate was placed within a ~0.1 T magnetic field, at 30° to the X-ray beam, resulting in a component of the magnetic field parallel

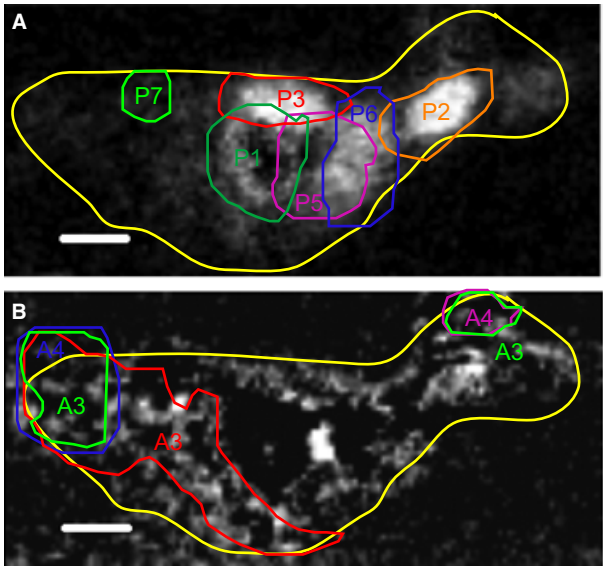

Fig. 4 (A) protein component map and (B) polysaccharide component map (both from Fig. 2) overlaid by contours defining areas from which Fe $L_{2,3}$-edge X-ray absorption spectral were extracted to generate X-ray magnetic circular dichroism spectra (Fig. 5), these were for either the whole area (yellow contour) or high concentrations of either (A) protein/lipid (P1-P7) or (B) polysaccharide (A1–A4). Scale bar is 500 nm for both images.

to the beam direction whilst also allowing the beam to pass through the sample into the detector. Two Fe $L_{2,3}$-edge stacks were collected, one with left and the other with RCP X-rays, thus providing two XAS per image pixel; the XMCD is obtained as the difference between these two spectra. The average XAS and XMCD spectra for the sample area within the yellow contour of Fig. 4 are shown in Fig. 3Bi. The average XAS and XMCD spectra obtained for this sample is compared to Fe $L_{2,3}$ spectra previously taken in total-electron yield (TEY) on beamline 4.0.2 at the Advanced Light Source (ALS) for a similar sample of biomagnetite produced by the same bacterium (Fig. 3Bii), published in Coker *et al.* (2007). In that study, the two XAS were obtained by switching the magnetic field between a parallel and anti-parallel direction along the incident X-ray beam.

It can be seen from Fig. 3B that the magnitude of the STXM–XMCD signal is smaller than that in the TEY–XMCD measurement. This can be ascribed in part to the fact that the sample is mounted at 30° to the X-ray beam, and so only 50% of the XMCD signal is observed. Also, there is a lower magnetisation of the sample in the STXM–XMCD measurement, where a smaller magnetic field had to be applied owing to the space constraints of the STXM chamber. However, the smaller magnitude does not affect the overall shape of the XMCD signal, but merely leads to weaker signal and thus relatively larger increased noise in the spectra. The STXM–XMCD was collected in transmission mode giving the bulk mineralogy of the sample, whereas the XMCD taken from Coker *et al.* (2007) was collected in TEY mode which only probes the top 4–6 nm of the sample surface. Therefore, the two measurements allow us to compare the bulk and surface of the magnetite. The peak fitting results of the XMCD spectra, derived from non-linear least-squares fitting using calculated spectra for each of the three Fe environments (van der Laan & Kirkman, 1992; Pattrick *et al.*, 2002), are given in Table 1. These results indicate that the surface and bulk measurements are in reasonably good agreement particularly with respect to

Table 1 Results for the relative amounts of octahedral Fe(II), tetrahedral Fe(III) and octahedral Fe(III) as obtained by fitting the Fe $L_{2,3}$-edge XMCD spectra shown in Fig. 5 collected from the corresponding areas in Fig. 4 [whole area (yellow contour) or P = protein/lipid and A = polysaccharide]

Area	Fe(II) O_h*	Fe(III) T_d*	Fe(III) O_h*	Total	Fe(II)/Fe(III)	Absolute error in Fe(II)/Fe(III) ratio	T_d/O_h
Stoichiometric magnetite	1.00	1.00	1.00	3.00	0.50	0.020	0.50
Whole area	1.08	1.00	1.15	3.23	0.50	0.021	0.45
P1	1.33	1.00	1.11	3.45	0.63	0.022	0.41
P2	1.26	1.00	0.97	3.23	0.64	0.023	0.45
P3	1.33	1.00	1.11	3.45	0.63	0.022	0.41
P5	1.63	1.00	0.99	3.61	0.82	0.027	0.38
P6	0.81	1.00	1.16	2.97	0.38	0.021	0.51
P7	1.08	1.00	0.92	3.00	0.56	0.025	0.50
Average P	1.24	1.00	1.04	3.28	0.61	0.023	0.44
A1	0.73	1.00	1.33	3.06	0.31	0.018	0.49
A2	0.68	1.00	0.82	2.50	0.37	0.023	0.67
A3	0.84	1.00	1.07	2.91	0.41	0.021	0.52
A4	0.44	1.00	1.78	3.23	0.16	0.011	0.45
Average A	0.68	1.00	1.25	2.92	0.30	0.017	0.52
Shewanella oneidensis MR-1 TEY–XMCD†	1.05	1.00	0.99	3.04	0.53	0.023	0.49

TEY, total-electron yield; XMCD, X-ray magnetic circular dichroism.
Errors are indicated in a separate column
*Errors are ±0.02.
†From Coker *et al.* (2007).

the overall percentage of Fe(II) in the magnetite. The surface contribution from 29 nm nanoparticles is a significant proportion [up to 80% assuming a probing depth of 60 Å –see Coker *et al.* (2007)] of the total signal; therefore, this similarity might be expected.

Areas of the Fe $L_{2,3}$-edge map found to be high in either protein/lipid or polysaccharide were chosen and labelled P1–P7 for protein/lipid-rich areas and A1–A4 for polysaccharide-rich areas in Fig. 4. XAS were extracted from the two Fe stacks, and the XMCD spectra calculated and then fit in the same way as described above (Fig. 5). The results listed in Table 1 indicate that areas of magnetite corresponding to the position of protein/lipid in the sample contain a larger amount of Fe(II) compared to stoichiometric magnetite, whereas areas of magnetite associated with polysaccharides are under-saturated in Fe(II) compared to stoichiometric magnetite. For the areas of biomagnetite closely associated with the bacterium, the average Fe(II)/Fe(III) ratio is 0.61 ± 0.03, the most reduced magnetite present, and much more reduced than the average value of 0.50–0.53. This is confirmation that direct contact with the cells is an efficient mechanism for reducing Fe(III) to Fe(II), recrystallising the Fe(III)-oxyhydroxide into an 'over-reduced' form of magnetite. The areas rich in polysaccharides give XMCD signals that have an average Fe(II)/Fe(III) value of 0.30 ± 0.03, which is much lower than that for stoichiometric magnetite, tending towards maghemite (γ-Fe_2O_3), and suggests that direct contact is required in these cultures for maximal levels of Fe(III) reduction, although enough Fe(II) is still generated to fully recrystallise the Fe(III)-oxyhydroxide to magnetite.

It has been shown previously that biogenic nanomagnetite is (overall) typically slightly oversaturated with Fe(II) compared to stoichiometric magnetite, and this is thought to be a function of the O_2-free environment that these bacteria require in order to use Fe(III) as an electron acceptor (Kukkadapu *et al.*, 2005; Coker *et al.*, 2007; Carvallo *et al.*, 2008). However, from the limited observations presented in this study, the situation is seen to be more complex, especially during the reduction process, and the mineralogical status of the magnetite depends on the local (nanoscale) interactions of the microbial cell with the mineral substrates. Although this work is only based upon analyses from one sample area, the results can be compared to work on Fe(II)-oxidising bacteria, where a gradient in the oxidation state of Fe was observed using STXM, indicating the progression of Fe(II) oxidation beyond the cell microenvironment (Miot *et al.*, 2009c). Here, the importance of bacterial cell–mineral contact in the bioreduction of solid-phase Fe(III) is demonstrated; the precise contribution of surface-localised cytochromes (Clarke *et al.*, 2011) or other mechanisms including extracellular appendages (Gorby *et al.*, 2006), soluble secreted electron shuttles (Newman & Kolter, 2000) such as flavins (von Canstein *et al.*, 2008) or electron flow through mineral assemblages (Wilkins *et al.*, 2007) are controversial and could be active in the process we describe. The changes in Fe(II) concentration across the sample has implications for the reactions and sorption processes in subsurface sediments and in bioremediation

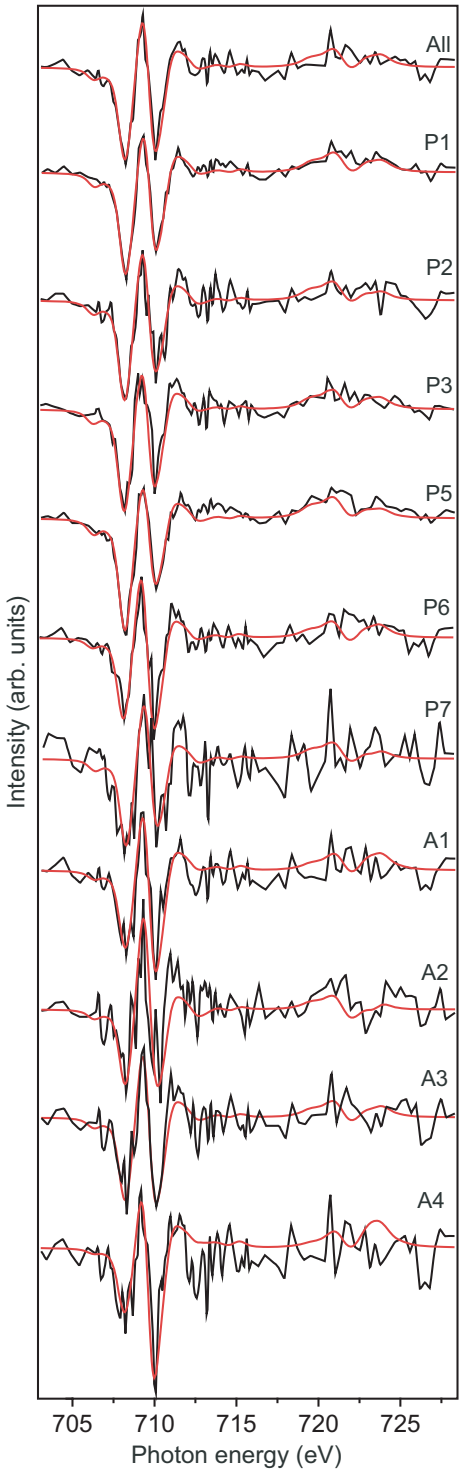

Fig. 5 Fe $L_{2,3}$-edge X-ray magnetic circular dichroism spectra (black) and the fits (red) corresponding to the areas of the carbon component images shown in Fig. 4.

approaches that are heavily dependent on the reducing power of the Fe(II) associated with Fe-biominerals, such as Cr(VI) reduction (Cutting *et al.*, 2010). During bioreduction, there is a very reduced magnetite component present that will be the major driver of toxic metal cycling and reduction and immobilisation of the metals (Ngomsik *et al.*, 2005). There will also be a maghemite-like component that is less reactive produced by other means such as electron mediator compounds. Future work could centre around investigating the differences in the Fe(II)/Fe(III) ratio across a sample when an electron mediator compound, such as a secreted flavin or a humic material, is introduced into the system.

The STXM–XMCD technique described here offers a unique combination of nano-scale (25 nm) spatial resolution and spectroscopic probing of the speciation of metals and lighter 'biological' elements such as carbon in dry and fully hydrated (Hitchcock *et al.*, 2009) samples. STXM provides direct imaging, quantification and correlation of the amounts (e.g. Wan *et al.*, 2007) and spatial localisation (e.g. Toner *et al.*, 2005; Hunter *et al.*, 2008; Chan *et al.*, 2009; Miot *et al.*, 2009b) of different components in environmental systems, which facilitates significant advances in our understanding of the mechanisms of many geomicrobiological processes, including the demonstration here that shows the potential of combining STXM with XMCD to identify the redox cycling of iron in both laboratory and potentially environmental samples.

ACKNOWLEDGMENTS

This work was supported by the NERC EnviroSync programme (UK), the Natural Sciences and Engineering Research Council of Canada (NSERC) and the Canada Research Chairs program. The authors would like to thank Karen Lam for assistance during beam time. Research described in this study was performed at the Canadian Light Source, which is supported by NSERC, the National Research Council Canada, the Canadian Institutes of Health Research, the Province of Saskatchewan, Western Economic Diversification Canada and the University of Saskatchewan.

REFERENCES

Ade H, Hitchcock AP (2008) NEXAFS microscopy and resonant scattering: composition and orientation probed in real and reciprocal space. *Polymer* **49**, 643–675.

Benzerara K, Yoon TH, Tyliszczak T, Constantz B, Spormann AM, Brown GE (2004) Scanning transmission X-ray microscopy study of microbial calcification. *Geobiology* **2**, 249–259.

Carvallo C, Sainctavit P, Arrio M-A, Menguy N, Wang Y, Ona-Nguema G, Brice-Profeta S (2008) Biogenic vs. abiogenic magnetite nanoparticles: a XMCD study. *American Mineralogist* **93**, 880–885.

Chan CS, Fakra SC, Edwards DC, Emerson D, Banfield JF (2009) Iron oxyhydroxide mineralization on microbial extracellual polysaccharides. *Geochimica et Cosmochimica Acta* **73**, 3807–3818.

Clarke TA, Edwards MJ, Gates AJ, Hall A, White GF, Bradley J, Reardon CL, Shi L, Beliaev AS, Marshall MJ, Wang Z, Watmough NJ, Fredrickson JK, Zachara JM, Butt JN, Richardson DJ (2011) Structure of a bacterial cell surface decaheme electron conduit. *Proceedings of the National Academy of Sciences* **108**, 9384–9389.

Coker VS, Pearce CI, Lang C, van der Laan G, Pattrick RAD, Telling ND, Schuler D, Arenholz E, Lloyd JR (2007) Cation site occupancy of biogenic magnetite compared to polygenic ferrite spinels determined by X-ray magnetic circular dichroism. *European Journal of Mineralogy* **19**, 707–716.

Coker VS, Telling ND, van der Laan G, Pattrick RAD, Pearce CI, Arenholz E, Tuna F, Winpenny REP, Lloyd JR (2009) Harnessing the extracellular bacterial production of nanoscale cobalt ferrite with exploitable magnetic properties. *ACS Nano* **3**, 1922–1928.

Cutting R, Coker VS, Telling ND, Kimber RL, Pearce CI, Ellis BL, Lawson RS, van der Laan G, Pattrick RAD, Vaughan DJ, Arenholz E, Lloyd JR (2010) Optimizing Cr(VI) and Tc(VII) remediation through nanoscale biomineral engineering. *Environmental Science and Technology* **44**, 2577–2584.

El-Naggar MY, Wanger G, Leung KM, Yuzvinsky TD, Southam G, Yang J, Lau WM, Nealson KH, Gorby YA (2010) Electrical transport along bacterial nanowires from *Shewanella oneidensis* MR-1. *Proceedings of the National Academy of Sciences* **107**, 18127–18131.

Fredrickson JK, Zachara JM, Kennedy DW, Dong H, Onstott TC, Hinman NW, Li S (1998) Biogenic iron mineralization accompanying the dissimilatory reduction of hydrous ferric oxide by groundwater bacterium. *Geochimica et Cosmochimica Acta* **62**, 3239–3257.

Gorby YA, Yanina S, McLean JS, Rosso KM, Moyles D, Dohnalkova A, Beveridge TJ, Chang IS, Kim BH, Kim KS, Culley DE, Reed SB, Romine MF, Saffarini DA, Hill EA, Shi L, Elias DA, Kennedy DW, Pinchuk G, Watanabe K, Ishii S, Logan B, Nealson KH, Fredrickson JK (2006) Electrically conductive bacterial nanowires produced by *Shewanella oneidensis* strain MR-1 and other microorganisms. *Proceedings of the National Academy of Sciences* **103**, 11358–11363.

Hitchcock AP (2011) aXis2000 is written in Interactive Data Language (IDL). It is available free for non-commercial use from http://unicorn.mcmaster.ca/aXis2000.html.

Hitchcock AP, Dynes JJ, Lawrence JR, Obst M, Swerhone GDW, Korber DR, Leppard GG (2009) Soft X-ray spectromicroscopy of nickel sorption in a natural river biofilm. *Geobiology* **7**, 432–453.

Hunter RC, Hitchcock AP, Dynes JJ, Obst M, Beveridge TJ (2008) Mapping the speciation of iron in pseudomonas aeruginosa biofilms using scanning transmission X-ray microscopy. *Environmental Science & Technology* **42**, 8766–8772.

Jacobsen C, Wirick S, Flynn G, Zimba C (2000) Soft X-ray spectroscopy from image sequences with sub-100nm spatial resolution. *Journal of Microscopy* **197**, 173–184.

Kaznatcheev KV, Karunakaran C, Lanke UD, Urquhart SG, Obst M, Hitchcock AP (2007) Soft X-ray spectromicroscopy beamline at the CLS commissioning results. *Nuclear Instruments & Methods in Physics Research A* **582**, 96–99.

Kukkadapu R, Zachara JM, Fredrickson JK, Kennedy DW, Dohnalkova A, McCready DE (2005) Ferrous hydroxy carbonate is a stable transformation product of biogenic magnetite. *American Mineralogist* **90**, 510–515.

Lam KP, Hitchcock AP, Obst M, Lawrence JR, Swerhone GDW, Leppard GG, Tyliszczak T, Karunakaran C, Wang J, Kaznatcheev K, Bazylinski DA, Lins U (2010) Characterizing magnetism of individual magnetosomes by X-ray magnetic circular dichroism in a scanning transmission X-ray microscope. *Chemical Geology* **270**, 110–116.

Lawrence JR, Swerhone GDW, Leppard GG, Araki T, Zhang X, West MM, Hitchcock AP (2003) Scanning transmission X-ray, laser scanning, and transmission electron microscopy mapping of the exopolymeric matrix of microbial biofilms. *Applied & Environmental Microbiology* **69**, 5543–5554.

Lloyd JR (2003) Microbial reduction of metals and radionuclides. *FEMS Microbiology Reviews* **27**, 411–425.

Lloyd JR, Leang C, Hodges Myerson AL, Coppi MV, Cuifo S, Methe B, Sandler SJ, Lovley DR (2003) Biochemical and genetic characterization of PpcA, a periplasmic *c*-type cytochrome in *Geobacter sulfurreducens*. *Biochemistry Journal* **369**, 153–161.

Lovley DR, Phillips EJP (1986) Availability of ferric iron for microbial reduction in bottom sediments of the freshwater tidal potomac river. *Applied & Environmental Microbiology* **52**, 751–757.

Lovley DR, Phillips EJP, Lonergan DJ (1989) Hydrogen and formate oxidisation coupled to dissimilatory reduction of iron or manganese by *Alteromonas putrefaciens*. *Applied & Environmental Microbiology* **55**, 700–706.

Lovley DR, Holmes DE, Nevin KP (2004) Dissimilatory Fe(III) and Mn(IV) reduction. *Advances in Microbial Physiology* **49**, 219–286.

Marsili E, Baron DB, Shikhare ID, Coursolle D, Gralnick JA, Bond DR (2008) Shewanella secretes flavins that mediate extracellular electron transfer. *Proceedings of the National Academy of Sciences* **105**, 3968–3973.

Miot J, Benzerara K, Morin G, Bernard S, Beyssac O, Larquet E, Kappler A, Guyot F (2009a) Transformation of vivianite by anaerobic nitrate-reducing iron-oxidizing bacteria. *Geobiology* **7**, 373–384.

Miot J, Benzerara K, Morin G, Kappler A, Bernard S, Obst M, Ferard C, Skouri-Panet F, Guigner JM, Posth N, Galvez M, Brown GE, Guyot F (2009b) Iron biomineralization by anaerobic neutrophilic iron-oxidizing bacteria. *Geochimica et Cosmochimica Acta* **73**, 696–711.

Miot J, Benzerara K, Obst M, Kappler A, Hegler F, Schadler S, Bouchez C, Guyot F, Morin G (2009c) Extracellular iron biomineralization by photoautotrophic iron-oxidizing bacteria. *Applied and Environmental Microbiology* **75**, 5586–5591.

Morrall P, Schedin F, Case GS, Thomas MF, Dudzik E, van der Laan G, Thornton G (2003) Stoichiometry of $Fe_{3-x}O_4$(111) ultrathin films on Pt(111). *Physical Review. B, Condensed Matter* **67**, 214408.

Myers CR, Myers JM (1992) Localisation of cytochromes to the outer membrane of anaerobically grown *Shewanella putrefaciens* MR-1. *Journal of Bacteriology* **174**, 3429–3438.

Nealson KH, Saffarini D (1994) Iron and manganese in anaerobic respiration: environmental significance, physiology, and regulation. *Annual Review of Microbiology* **48**, 311–343.

Newman DK, Kolter R (2000) A role for excreted quinones in extracellular electron transfer. *Nature* **405**, 94–97.

Ngomsik AF, Bee A, Draye M, Cote G, Cabuil V (2005) Magnetic nano- and microparticles for metal removal and environmental applications: a review. *Comptes Rendus Chimie* **8**, 963–970.

Ona-Nguema G, Abdelmoula M, Jorand F, Benali O, Gehin A, Block JC, Genin JMR (2002) Iron(II,III) hydroxycarbonate green rust formation and stabilization from lepidocrocite bioreduction. *Environmental Science & Technology* **36**, 16–20.

Pattrick RAD, van der Laan G, Henderson CMB, Kuiper P, Dudzik E, Vaughan DJ (2002) Cation site occupancy in spinel ferrites studied by X-ray magnetic circular dichroism: developing a method for mineralogists. *European Journal of Mineralogy* **14**, 1095–1102.

Ravindranath SP, Henne KL, Thompson DK, Irudayaraj J (2011) Surface-enhanced raman imaging of intracellular bioreduction of chromate in *Shewanella oneidensis*. *PLoS ONE* **6**, e16634.

Shi L, Squier TC, Zachara JM, Fredrickson JK (2007) Respiration of metal (hydr)oxides by Shewanella and Geobacter: a key role for multihaem c-type cytochromes. *Molecular Microbiology* **65**, 12–20.

Taillefert M, Beckler JS, Carey E, Burns JL, Fennessey CM, DiChristina TJ (2007) *Shewanella putrefaciens* produces an Fe(III)-solubilizing organic ligand during anaerobic respiration on insoluble Fe(III) oxides. *Journal of Inorganic Biochemistry* **101**, 1760–1767.

Toner B, Fakra S, Villalobos M, Warwick T, Sposito G (2005) Spatially resolved characterization of biogenic manganese oxide production within a bacterial biofilm. *Applied and Environmental Microbiology* **71**, 1300–1310.

van der Laan G, Kirkman IW (1992) The 2*p* absorption spectra of 3*d* transition metal compounds in tetrahedral and octahedral symmetry. *Journal of Physics: Condensed Matter* **4**, 4189–4204.

van der Laan G, Thole BT (1991) Strong magnetic x-ray dichroism in 2*p* absorption spectra of 3*d* transition metal ions. *Physical Review. B, Condensed Matter* **43**, 13401–13411.

von Canstein H, Ogawa J, Shimizu S, Lloyd JR (2008) Secretion of flavins by Shewanella species and their role in extracellular electron transfer. *Applied & Environmental Microbiology* **74**, 615–623.

Wan J, Tyliszczak T, Tokunaga TK (2007) Organic carbon distribution, speciation, and elemental correlations within soil microaggregates: applications of STXM and NEXAFS spectroscopy. *Geochimica et Cosmochimica Acta* **71**, 5439–5449.

Wilkins MJ, Wincott PL, Vaughan DJ, Livens FR, Lloyd JR (2007) Growth of *Geobacter sulfurreducens* on poorly crystalline Fe(III) oxyhydroxide coatings. *Geomicrobiology Journal* **3/4**, 199–204.

SUPPORTING INFORMATION

Additional Supporting Information may be found in the online version of this article:

Fig. S1 Schematic of the sample arrangement in the beam with the magnetic field and beam direction indicated.

Please note: Wiley-Blackwell are not responsible for the content or functionality of any supporting materials supplied by the authors. Any queries (other than missing material) should be directed to the corresponding author for the article.